Research Article | Vol. 8, No. 10 | 1 Oct 2017 | BIOMEDICAL OPTICS EXPRESS 4706
Biomedical Optics EXPRESS

In vivo cellular-level real-time pharmacokinetic imaging of free-form and liposomal indocyanine green in liver

YOONHA HWANG,[1,2] HWANJUN YOON,[2,3] KIBAEK CHOE,[1,2] JINHYO AHN,[1,2] JIK HAN JUNG,[2,3] JI-HO PARK,[2,3] AND PILHAN KIM[1,2,*]

[1]*Graduate School of Nanoscience and Technology, Korea Advanced Institute of Science and Technology (KAIST), 291 Deahak-ro, Yuseong-gu, Daejeon, 34141, South Korea*
[2]*KI for Health Science and Technology (KIHST), Korea Advanced Institute of Science and Technology (KAIST), 291 Deahak-ro, Yuseong-gu, Daejeon, 34141, South Korea*
[3]*Department of Bio and Brain Engineering, Korea Advanced Institute of Science and Technology (KAIST), 291 Deahak-ro, Yuseong-gu, Daejeon, 34141, South Korea*
[*]*pilhan.kim@kaist.ac.kr*

Abstract: Indocyanine green (ICG) is a near-infrared fluorophore approved for human use which has been widely used for various clinical applications. Despite the well-established clinical usage, our understanding about the microscopic *in vivo* pharmacokinetics of systemically administered ICG has been relatively limited. In this work, we successfully visualized real-time *in vivo* pharmacokinetic dynamics of the intravenously injected free-form and liposomal ICG in cellular resolution by utilizing a custom-built video-rate near infrared laser-scanning confocal microscopy system. Initial perfusion and clearance from blood stream, diffusion into perisinusoidal space, and subsequent absorption into hepatocyte were directly visualized *in vivo*. The quantification analysis utilizing the real-time image sequences revealed distinct dynamic *in vivo* pharmacokinetic behavior of free-form and liposomal ICG.

OCIS codes: (170.3880) Medical and biological imaging; (170.0170) Medical optics and biotechnology; (170.1790) Confocal microscopy; (170.2520) Fluorescence microscopy.

References and links

1. T. Iijima, T. Aoyagi, Y. Iwao, J. Masuda, M. Fuse, N. Kobayashi, and H. Sankawa, "Cardiac output and circulating blood volume analysis by pulse dye-densitometry," J. Clin. Monit. **13**(2), 81–89 (1997).
2. O. Okochi, T. Kaneko, H. Sugimoto, S. Inoue, S. Takeda, and A. Nakao, "ICG pulse spectrophotometry for perioperative liver function in hepatectomy," J. Surg. Res. **103**(1), 109–113 (2002).
3. T. Desmettre, J. M. Devoisselle, and S. Mordon, "Fluorescence properties and metabolic features of indocyanine green (ICG) as related to angiography," Surv. Ophthalmol. **45**(1), 15–27 (2000).
4. A. M. Smith, M. C. Mancini, and S. Nie, "Bioimaging: Second window for in vivo imaging," Nat. Nanotechnol. **4**(11), 710–711 (2009).
5. R. Weissleder, "A clearer vision for in vivo imaging," Nat. Biotechnol. **19**(4), 316–317 (2001).
6. J. V. Frangioni, "In vivo near-infrared fluorescence imaging," Curr. Opin. Chem. Biol. **7**(5), 626–634 (2003).
7. V. Ntziachristos, C. Bremer, and R. Weissleder, "Fluorescence imaging with near-infrared light: new technological advances that enable in vivo molecular imaging," Eur. Radiol. **13**(1), 195–208 (2003).
8. B. E. Schaafsma, J. S. D. Mieog, M. Hutteman, J. R. van der Vorst, P. J. K. Kuppen, C. W. G. M. Löwik, J. V. Frangioni, C. J. H. van de Velde, and A. L. Vahrmeijer, "The Clinical Use of Indocyanine Green as a near-Infrared Fluorescent Contrast Agent for Image-Guided Oncologic Surgery," J. Surg. Oncol. **104**(3), 323–332 (2011).
9. S. Kwon, G. D. Agollah, G. Wu, W. Chan, and E. M. Sevick-Muraca, "Direct visualization of changes of lymphatic function and drainage pathways in lymph node metastasis of B16F10 melanoma using near-infrared fluorescence imaging," Biomed. Opt. Express **4**(6), 967–977 (2013).
10. R. Sharma, W. Wang, J. C. Rasmussen, A. Joshi, J. P. Houston, K. E. Adams, A. Cameron, S. Ke, S. Kwon, M. E. Mawad, and E. M. Sevick-Muraca, "Quantitative imaging of lymph function," Am. J. Physiol. Heart Circ. Physiol. **292**(6), H3109–H3118 (2007).
11. N. Unno, M. Nishiyama, M. Suzuki, N. Yamamoto, K. Inuzuka, D. Sagara, H. Tanaka, and H. Konno, "Quantitative lymph imaging for assessment of lymph function using indocyanine green fluorescence lymphography," Eur. J. Vasc. Endovasc. Surg. **36**(2), 230–236 (2008).
12. C. Holm, M. Mayr, E. Höfter, A. Becker, U. J. Pfeiffer, and W. Mühlbauer, "Intraoperative evaluation of skin-flap viability using laser-induced fluorescence of indocyanine green," Br. J. Plast. Surg. **55**(8), 635–644 (2002).

#302997 https://doi.org/10.1364/BOE.8.004706
Journal © 2017 Received 21 Jul 2017; revised 13 Sep 2017; accepted 15 Sep 2017; published 26 Sep 2017

Biomedical Optics EXPRESS

13. C. Habermehl, C. H. Schmitz, and J. Steinbrink, "Contrast enhanced high-resolution diffuse optical tomography of the human brain using ICG," Opt. Express **19**(19), 18636–18644 (2011).
14. T. Holmes, A. Invernizzi, S. Larkin, and G. Staurenghi, "Dynamic indocyanine green angiography measurements," J. Biomed. Opt. **17**(11), 116028 (2012).
15. M. Choi, K. Choi, S. W. Ryu, J. Lee, and C. Choi, "Dynamic fluorescence imaging for multiparametric measurement of tumor vasculature," J. Biomed. Opt. **16**(4), 046008 (2011).
16. Y. Kang, M. Choi, J. Lee, G. Y. Koh, K. Kwon, and C. Choi, "Quantitative Analysis of Peripheral Tissue Perfusion Using Spatiotemporal Molecular Dynamics," PLoS One **4**(1), e4275 (2009).
17. N. L. Martirosyan, D. D. Cavalcanti, J. M. Eschbacher, P. M. Delaney, A. C. Scheck, M. G. Abdelwahab, P. Nakaji, R. F. Spetzler, and M. C. Preul, "Use of in vivo near-infrared laser confocal endomicroscopy with indocyanine green to detect the boundary of infiltrative tumor Laboratory investigation," J. Neurosurg. **115**(6), 1131–1138 (2011).
18. W. Piyawattanametha, H. Ra, Z. Qiu, S. Friedland, J. T. C. Liu, K. Loewke, G. S. Kino, O. Solgaard, T. D. Wang, M. J. Mandella, and C. H. Contag, "In vivo near-infrared dual-axis confocal microendoscopy in the human lower gastrointestinal tract," J. Biomed. Opt. **17**(2), 021102 (2012).
19. H. Skvara, H. Kittler, J. A. Schmid, U. Plut, and C. Jonak, "In vivo fluorescence confocal microscopy: indocyanine green enhances the contrast of epidermal and dermal structures," J. Biomed. Opt. **16**(9), 096010 (2011).
20. S. T. Proulx, P. Luciani, S. Derzsi, M. Rinderknecht, V. Mumprecht, J. C. Leroux, and M. Detmar, "Quantitative Imaging of Lymphatic Function with Liposomal Indocyanine Green," Cancer Res. **70**(18), 7053–7062 (2010).
21. A. Gabizon and D. Papahadjopoulos, "Liposome Formulations with Prolonged Circulation Time in Blood and Enhanced Uptake by Tumors," Proc. Natl. Acad. Sci. U.S.A. **85**(18), 6949–6953 (1988).
22. W. T. Song, Z. H. Tang, D. W. Zhang, N. Burton, W. Driessen, and X. S. Chen, "Comprehensive studies of pharmacokinetics and biodistribution of indocyanine green and liposomal indocyanine green by multispectral optoacoustic tomography," Rsc Adv **5**(5), 3807–3813 (2015).
23. C. Zheng, M. Zheng, P. Gong, D. Jia, P. Zhang, B. Shi, Z. Sheng, Y. Ma, and L. Cai, "Indocyanine green-loaded biodegradable tumor targeting nanoprobes for in vitro and in vivo imaging," Biomaterials **33**(22), 5603–5609 (2012).
24. K. Kono, M. Takashima, E. Yuba, A. Harada, Y. Hiramatsu, H. Kitagawa, T. Otani, K. Maruyama, and S. Aoshima, "Multifunctional liposomes having target specificity, temperature-triggered release, and near-infrared fluorescence imaging for tumor-specific chemotherapy," J. Control. Release **216**, 69–77 (2015).
25. J. Zheng, N. Muhanna, R. De Souza, H. Wada, H. Chan, M. K. Akens, T. Anayama, K. Yasufuku, S. Serra, J. Irish, C. Allen, and D. Jaffray, "A multimodal nano agent for image-guided cancer surgery," Biomaterials **67**, 160–168 (2015).
26. A. K. Rengan, M. Jagtap, A. De, R. Banerjee, and R. Srivastava, "Multifunctional gold coated thermo-sensitive liposomes for multimodal imaging and photo-thermal therapy of breast cancer cells," Nanoscale **6**(2), 916–923 (2014).
27. A. Yuan, X. Tang, X. Qiu, K. Jiang, J. Wu, and Y. Hu, "Activatable photodynamic destruction of cancer cells by NIR dye/photosensitizer loaded liposomes," Chem. Commun. (Camb.) **51**(16), 3340–3342 (2015).
28. F. Yan, H. Wu, H. Liu, Z. Deng, H. Liu, W. Duan, X. Liu, and H. Zheng, "Molecular imaging-guided photothermal/photodynamic therapy against tumor by iRGD-modified indocyanine green nanoparticles," J. Control. Release **224**, 217–228 (2016).
29. G. Zhang, F. Liu, B. Zhang, Y. He, J. Luo, and J. Bai, "Imaging of pharmacokinetic rates of indocyanine green in mouse liver with a hybrid fluorescence molecular tomography/x-ray computed tomography system," J. Biomed. Opt. **18**(4), 040505 (2013).
30. X. Liu, X. L. Guo, F. Liu, Y. Zhang, H. Zhang, G. S. Hu, and J. Bai, "Imaging of Indocyanine Green Perfusion in Mouse Liver With Fluorescence Diffuse Optical Tomography," IEEE Trans. Biomed. Eng. **58**, 2139–2143 (2011).
31. A. Taruttis, S. Morscher, N. C. Burton, D. Razansky, and V. Ntziachristos, "Fast Multispectral Optoacoustic Tomography (MSOT) for Dynamic Imaging of Pharmacokinetics and Biodistribution in Multiple Organs," PLoS One **7**(1), e30491 (2012).
32. S. Patwardhan, S. Bloch, S. Achilefu, and J. Culver, "Time-dependent whole-body fluorescence tomography of probe bio-distributions in mice," Opt. Express **13**(7), 2564–2577 (2005).
33. J. T. Alander, I. Kaartinen, A. Laakso, T. Pätilä, T. Spillmann, V. V. Tuchin, M. Venermo, and P. Välisuo, "A review of indocyanine green fluorescent imaging in surgery," Int. J. Biomed. Imaging **2012**, 940585 (2012).
34. C. M. Leevy, F. Smith, J. Longueville, G. Paumgartner, and M. M. Howard, "Indocyanine green clearance as a test for hepatic function. Evaluation by dichromatic ear densitometry," JAMA **200**(3), 236–240 (1967).
35. R. L. Lindquist, G. Shakhar, D. Dudziak, H. Wardemann, T. Eisenreich, M. L. Dustin, and M. C. Nussenzweig, "Visualizing dendritic cell networks in vivo," Nat. Immunol. **5**(12), 1243–1250 (2004).
36. S. Jung, J. Aliberti, P. Graemmel, M. J. Sunshine, G. W. Kreutzberg, A. Sher, and D. R. Littman, "Analysis of fractalkine receptor CX(3)CR1 function by targeted deletion and green fluorescent protein reporter gene insertion," Mol. Cell. Biol. **20**(11), 4106–4114 (2000).
37. M. Rajadhyaksha, R. R. Anderson, and R. H. Webb, "Video-rate confocal scanning laser microscope for imaging human tissues in vivo," Appl. Opt. **38**(10), 2105–2115 (1999).
38. I. Veilleux, J. A. Spencer, D. P. Biss, D. Cote, and C. P. Lin, "In vivo cell tracking with video rate multimodality laser scanning microscopy," IEEE J. Sel. Top. Quantum Electron. **14**(1), 10–18 (2008).

Biomedical Optics EXPRESS

39. Y. Hwang, J. Ahn, J. Mun, S. Bae, Y. U. Jeong, N. A. Vinokurov, and P. Kim, "In vivo analysis of THz wave irradiation induced acute inflammatory response in skin by laser-scanning confocal microscopy," Opt. Express **22**(10), 11465–11475 (2014).
40. H. Seo, Y. Hwang, K. Choe, and P. Kim, "In vivo quantitation of injected circulating tumor cells from great saphenous vein based on video-rate confocal microscopy," Biomed. Opt. Express **6**(6), 2158–2167 (2015).
41. K. Choe, J. Y. Jang, I. Park, Y. Kim, S. Ahn, D. Y. Park, Y. K. Hong, K. Alitalo, G. Y. Koh, and P. Kim, "Intravital imaging of intestinal lacteals unveils lipid drainage through contractility," J. Clin. Invest. **125**(11), 4042–4052 (2015).
42. E. Song, H. Seo, K. Choe, Y. Hwang, J. Ahn, S. Ahn, and P. Kim, "Optical clearing based cellular-level 3D visualization of intact lymph node cortex," Biomed. Opt. Express **6**(10), 4154–4164 (2015).
43. F. Heymann and F. Tacke, "Immunology in the liver--from homeostasis to disease," Nat. Rev. Gastroenterol. Hepatol. **13**(2), 88–110 (2016).
44. B. Janssen, J. Debets, P. Leenders, and J. Smits, "Chronic measurement of cardiac output in conscious mice," Am. J. Physiol. Regul. Integr. Comp. Physiol. **282**(3), R928–R935 (2002).
45. L. Prodanov, R. Jindal, S. S. Bale, M. Hegde, W. J. McCarty, I. Golberg, A. Bhushan, M. L. Yarmush, and O. B. Usta, "Long-term maintenance of a microfluidic 3D human liver sinusoid," Biotechnol. Bioeng. **113**(1), 241–246 (2016).
46. J. C. Ryan, K. W. Dunn, and B. S. Decker, "Effects of chronic kidney disease on liver transport: quantitative intravital microscopy of fluorescein transport in the rat liver," Am. J. Physiol. Regul. Integr. Comp. Physiol. **307**(12), R1488–R1492 (2014).

1. Introduction

Indocyanine green (ICG) is a biocompatible fluorophore approved for human use by U.S. Food and Drug Administration (FDA). ICG has been widely used for various clinical applications such as determination of cardiac output [1], liver function diagnostics [2], and ophthalmic angiography [3]. In addition to the biocompatibility, as a near infrared (NIR) fluorophore with the emission peak around 800 nm, ICG provides several advantages for *in vivo* fluorescence imaging of human tissue. Auto-fluorescence background and light scattering of the biological tissue are much smaller in the NIR wavelength region than those in the visible wavelength region, which is beneficial to achieve the higher signal-to-noise ratio (SNR) and the deeper imaging depth in the living human tissue with less photo-damage [4–7]. Recently, novel clinical applications utilizing the favorable characteristics of ICG for NIR fluorescence imaging have been actively investigated, which includes image-guided surgery [8], quantitative monitoring of lymphatic function [9–11], and dynamic evaluation of vascular perfusion in skin [12], brain [13], retina [14], tumor [15] and peripheral tissue [16]. In addition, a cellular-level visualization of brain tumor [17], gastrointestinal tract [18] and human skin [19] using a confocal microscopy or endomicroscopy was demonstrated. In addition, over the last decade, the ICG encapsulated in the artificially-prepared spherical vesicle composed of a biocompatible lipid bilayer, termed as liposomal ICG, has been actively developed. Liposomal ICG is reported to have several advantages over free-form ICG such as improved stability in solution [20], prolonged retention in blood circulation [21, 22], and enhanced accumulation and retention in tumor [22]. These characteristics suggest the usefulness of the liposomal ICG not only for *in vivo* NIR fluorescence imaging, but also for cancer detection [23–25] and treatment potentially by photo-thermal therapy [26–28].

Despite the well-established clinical usage of the ICG and active investigations to utilize the liposomal ICG for novel clinical applications, the dynamic distribution of them after the systemic introduction into the body has been investigated mostly in macroscopic tissue scale and in relatively long-term time scale of several hours to days [20, 22, 29–32]. As the free-form ICG introduced into the human body via intravenous injection in most clinical applications is known to be rapidly cleared out from the blood plasma after several minutes [33], it is desirable to analyze the dynamic pharmacokinetics of ICG during the similar time period of initial several minutes accordingly. In addition, although it has been known that the metabolic clearance of ICG from the blood mostly occurs in the liver [34], revealed by real-time monitoring in macroscopic organ scale [22, 29–32], a dynamic clearance process of ICG from the liver sinusoid to perisinusoidal space, subsequent cellular-level absorption and distribution in the stromal liver hepatocyte under *in vivo* environment have not been well understood. It is partially due to the lack of appropriate ICG imaging technique which requires the cellular resolution and fast real-time imaging speed.

Biomedical Optics EXPRESS

In this work, we implemented a video-rate confocal NIR laser-scanning microscopy system, which is capable of a real-time intravital confocal imaging of ICG fluorescence at the speed of 30 frames per second *in vivo*. Using the imaging system for a live mouse model with tail-vein catheterization, the rapid pharmacokinetic dynamics of the intravenously administered free-form ICG and liposomal ICG were directly observed *in vivo* at the peripheral tissue, skin, and the major metabolic organ, liver. First, in the ear skin, the gradual mixing dynamics of the injected ICG in circulating blood in the first 30 seconds was observed with both free-form and liposomal ICG, which is revealed by the sequential appearance of ICG fluorescence in the artery and vein. After 1 hour, the extended retention of the liposomal ICG in blood circulation was clearly observed. Second, in the liver, dynamic pharmacokinetic processes of intravenously administered free-form ICG and liposomal ICG including the initial perfusion to liver sinusoid, diffusion into perisinusoidal space, and subsequent absorption into the hepatocyte were observed in real-time for the initial 5 minutes. Similar to the results observed in the skin, the increased retention in blood circulation of liposomal ICG than the free-form ICG was observed while no significant difference in the initial absorption into hepatocyte was observed. However, after 12 hours, the liposomal ICG captured by the liver-resident Kupffer cell was clearly visible while no fluorescence signal was observed from the liver of free-form ICG injected mouse.

2. Methods

2.1 Animal model preparation for the imaging

Eight weeks old BALB/c mice were purchased from Orient Bio Inc. (Seongnam, Korea). CD11c-YFP (Stock no. #008829 [35]), CX3CR1-GFP (Stock no. #005582 [36]), were purchased from Jackson Laboratory (Bar Harbor, USA). Mice were anesthetized by intramuscular injection of a mixture of zoletil (30 mg/kg) and xylazine (10 mg/kg). The skin was shaved by hair removal cream before the imaging or surgical procedure. The liver was surgically exposed by a small incision in the skin and peritoneum for the imaging of ICG pharmacokinetic dynamics. The ICG fluorescence imaging was performed at the depth of 30 μm from the tissue surface where blood vessels or liver sinusoids were clearly observed. The 785nm near-infrared laser intensity illuminated on the tissue for ICG fluorescence imaging was 0.337mW. 200 μl of free-form ICG solution (60 μM) or liposomal ICG (60 μM) solution was intravenously administered through the tail vein catheter. To obtain high subcellular-level resolution images of liver *in vivo*, an averaging of multiple frames acquired in video-rate was performed with frame by frame registration to compensate the motion of liver tissue. During the imaging, the body temperature was maintained at 36 °C by using a homeothermic control system (PhysioSuiteTM, RightTemp, Kent Scientific). This study was carried out in accordance with the ARRIVE (Animal Research: Reporting *In Vivo* Experiments) guidelines. All animal experiments were performed in accordance with the protocol approved by the Animal Care Committee of KAIST (protocol no. KA2014-14). All surgical procedures were performed under anesthesia, and all efforts were made to minimize the suffering.

2.2 Near-infrared laser-scanning confocal microscopy system

For *in vivo* video-rate cellular-level monitoring of ICG pharmacokinetic dynamics, a custom-built video-rate laser-scanning confocal microscopy system previously described [37–42] was modified for simultaneous imaging of green and near infrared ICG fluorescence imaging as shown in Fig. 1(a). Continuous-wave laser modules at 488 and 785 nm (OBIS, Coherent) were used as an excitation source. The laser beams reflected by right-angle dichroic beam splitters (DBS1; FF801-Di01, DBS2; FF495-Di03, Semrock) was delivered to a 2D raster-pattern scanner composed by a rotating 36 facet polygonal mirror (MC-5, gold coated, Lincoln Laser) and a galvanometer based scanning mirror (6230H, Cambridge Technology). The scanning laser beam was delivered to the anesthetized mouse on XYZ translation stage (3DMS, Sutter Instrument) through a commercial long working distance objective lens (LUCPlanFL, 20X, 0.45NA, Olympus) providing the field of views of 600 × 600 μm^2. The

Biomedical Optics EXPRESS

fluorescence signal collected by the objective lens in epi-detection manner was descanned and then separated from the excitation laser beam by the dichroic beam splitters (DBS1; FF801-Di01, DBS2; FF495-Di03, DBS3; FF560-Di01, Semrock). Photomultiplier tubes (PMT; R9110, Hamamatsu) were used to detect the fluorescence signal through each band pass filter (BPF1; FF01-835/70, BPF2; FF525/50, Semrock). The electronic outputs from the PMT were digitized by a frame grabber (Solios, Matrox) with a sampling rate of 10 MHz. Image with the size of 512 × 512 pixels was displayed and recorded in real time at a frame rate of 30 Hz by using a custom-written imaging software based on Matrox Imaging Library (MIL9, Matrox).

2.3 Preparation of free-from and liposomal ICG

For the preparation of liposomal ICG, a lipid cake was prepared with L-α-phosphatidylcholine, hydrogenated (Soy) (HSPC, Avanti Polar Lipids) and 1,2-distearoyl-sn-glycero-3-phosphoethanolamine-N-[methoxy(polyethylene glycol)-2000] (DSPE-PEG, Avanti Polar Lipids) at the molar ratio of 95:5 and added ICG (Tokyo Chemical Industry CO. LTD.) at the molar ratio of 250:1 (total lipids:ICG). And then, the organic solvent was evaporated. The film was then hydrated with 5% glucose solution (w/v) at 60 °C. After the hydration and membrane (100 nm) extrusion, the remained free-form ICG was removed by size-exclusion chromatography (GE Healthcare) and dialysis (Spectrum Labs). The final concentration of ICG loaded in the liposomes was 60 μM which determined by measuring the absorbance at 785 nm after mixing the liposome solution with methanol at the volume ratio of 2:8. The free-form ICG solution was prepared at the same concentration as the liposomal ICG.

3. Result

3.1 Video-rate imaging analysis of the free-form and liposomal ICG in the blood circulation

The schematic of the imaging system capable of video-rate confocal image acquisition at the speed of 30 frames per second is shown in Fig. 1(a). Figure 1(b) and 1(c) are representative images obtained at the ear skin of free-form ICG injected mouse, which demonstrates the *in vivo* ICG imaging capability of the system. Immediately after the intravenous injection of free-form ICG, we successfully visualized the blood vessel in the dermis as shown in Fig. 1(b). At 30 minutes after the injection, ICG fluorescence is no more detectable in the blood circulation. On the other hand, with the injection of 20 times more amount of free-form ICG, we could observe the lymphatic vessel draining ICG at 30 minutes after the injection as shown in Fig. 1(c), because the portion of the injected free-form ICG was leaked out from the blood vessel to the dermal skin tissue and then drained through the lymphatic vessel.

Biomedical Optics EXPRESS

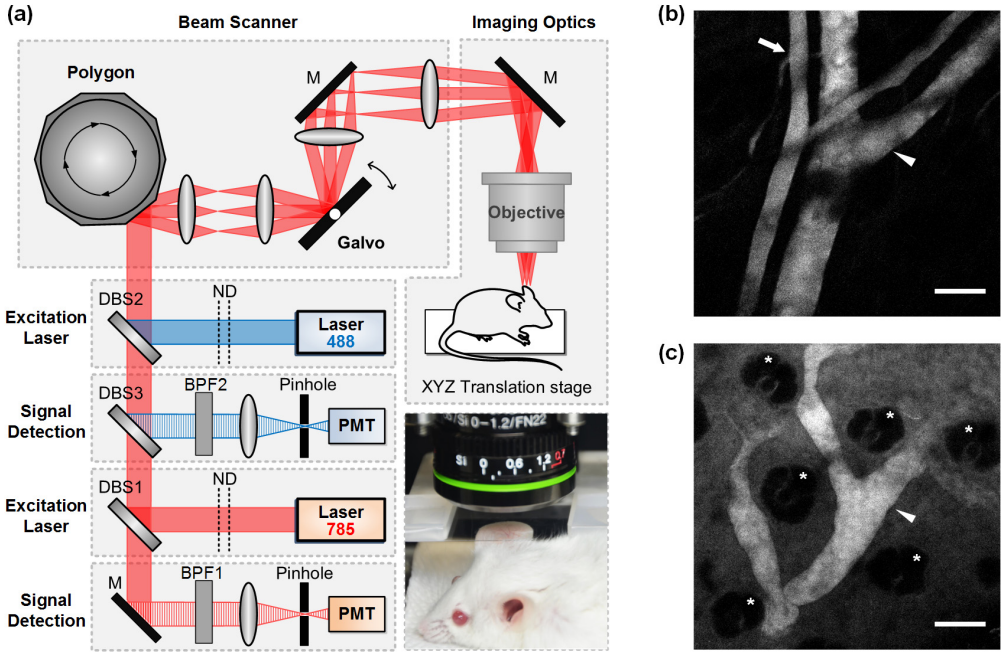

Fig. 1. (a) Schematic of laser-scanning confocal microscopy: DBS, dichroic beam splitter; BPF, band pass filter; ND, neutral density filter; M, mirror; PMT, photomultiplier tube. Photograph shows an anesthetized live mouse prepared for ear skin imaging, *in vivo*. (b, c) The representative images acquired at the ear skin of mouse after the intravenous injection of ICG. (b) At immediately after the ICG injection, blood vessels were visible. The artery (arrow) and vein (arrow head) were distinguishable by the vessel diameter and blood flow speed. (c) At 30 minutes after the ICG injection, the lymphatic vessel (arrow head) draining ICG leaked from the blood vessel to dermal tissue was visible. The hair follicle (asterisk) was also distinguishable. Scale bar: 100 μm.

To compare the rapid dynamic change in the blood circulation of free-form ICG and liposomal ICG, the blood vessel in peripheral tissue, skin, was monitored in real-time immediately after the intravenous injection *in vivo*. The imaging of the blood vessel was performed in the ear skin due to the ease of the accessibility and demobilization of the tissue under imaging as shown in Fig. 1(a). To observe the initial pharmacokinetics in the blood stream immediately after the injection, the continuous video-rate movie recording started simultaneously with the intravenous injection of free-form ICG or liposomal ICG through the catheter inserted into the mouse tail vein (Visualization 1 and Visualization 2).

Figure 2(a) is the representative sequential images showing the dynamic changes of the injected free-form ICG and liposomal ICG in the blood circulation. To note, artery and vein, distinguishable by vessel diameter and flow speeds, are pseudo-colored in red and blue, respectively. Figure 2(b) is the graphs showing the dynamically changing fluorescence signal of free-form and liposomal ICG observed in the blood vessels of ear skin (Visualization 1 and Visualization 2). The fluorescence signal intensity was directly measured from the video-rate image sequences with the speed of 30 frames per second by calculating the average of the area of artery and the vein shown in Fig. 2(a), excluding overlapping area and shadowed area by hair follicle. For the both of free-form ICG and liposomal ICG, the ICG fluorescence signal appeared in the artery of ear skin within around 4 seconds after the injection, then rapidly increased and reached the peak at around 7 seconds. Notably, it took only 2.5 seconds to increase from the 10% intensity to reach the maximum peak value, then 3 seconds to decrease to 50% intensity. After the initial peak, the ICG fluorescence signal in the artery continuously decreased as the injected ICG solution with the volume of 200 μl was gradually mixed with the whole blood of the mouse while circulating the whole body. Subsequently, the ICG fluorescence signal started to appear in the vein after passing through the capillary

Biomedical Optics EXPRESS

network in the periphery and reached the peak at around 25 seconds after the injection then gradually decreased in the similar pattern with the artery. In comparison, the fluorescence signal in the vein increased in 4 times slower speed than that in the artery, and the peak intensity was also lower.

During the initial 1 minute, there was no significant difference in blood circulating dynamics between free-form ICG and liposomal ICG. After 1 minute, the fluorescence signal of free-form ICG quickly decreased as shown in Fig. 2(b). At 5 minutes after the injection, the fluorescence signal of free-form ICG was decreased to the value less than 5% of the maximum peak intensity in both of artery and vein, suggesting almost complete clearance from the blood circulation. In contrast, after 1 minute, the fluorescence signal of liposomal ICG decrease much slowly and maintained more than 30% of the peak intensity at 5 minutes after the injection. After 1 hour, the liposomal ICG continued to remain in the blood circulation as shown in Fig. 2(a), suggesting significantly improved retention in blood stream.

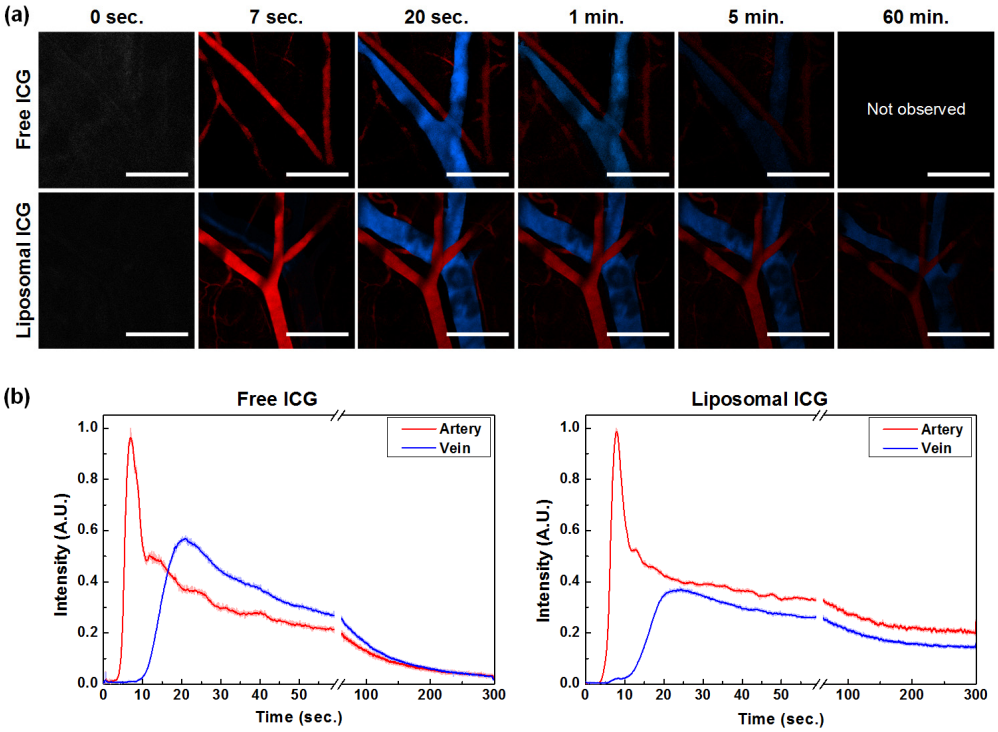

Fig. 2. (a) Representative sequential images of the peripheral blood vessel in the ear skin of the mouse intravenously administered free-form and liposomal ICG, respectively (Visualization 1 and Visualization 2). Artery and vein are pseudo-colored in red and blue, respectively. (b) The real-time changes of the ICG fluorescence signal in peripheral blood vessel in the ear skin after the intravenous administration of free-form ICG and liposomal ICG. Scale bar: 250 μm.

3.2 Video-rate cellular-level imaging analysis of free-form and liposomal ICG in the liver

To compare the pharmacokinetics of free-form and liposomal ICG in the liver which is known to play a major role in the metabolism of the ICG administered into the human body, a video-rate cellular-level imaging was performed. The continuous video-rate movie recording started simultaneously with the intravenous injection of free-form ICG or liposomal ICG. As shown in the Fig. 3(a), the initial pharmacokinetic behavior of the intravenously injected free-form and liposomal ICG in the liver were successfully visualized (Visualization 3 and Visualization 4). Figure 3(b) is the magnified sequential images obtained at the areas marked by yellow squares in Fig. 3(a). Dynamic pharmacokinetic behaviors such as initial perfusion

Biomedical Optics EXPRESS

in liver sinusoid, gradual diffusion into perisinusoidal space and subsequent absorption into hepatocytes are clearly visualized (Visualization 5 and Visualization 6). Figure 3(c) shows the fluorescence signal intensity in liver sinusoid, which was obtained by calculating the average of four different sinusoids branches with length of 50-100 μm. For both of free-form and liposomal ICG, the fluorescence signal in the liver sinusoid appeared at around 12 seconds, then gradually increased and reached the peak at around 27 seconds after the injection, which was almost similar to the dynamic fluorescence signal change observed in the vein of ear skin. Interestingly, while the fluorescence signal in the lumen decreased, a highly concentrated ICG signal was observed at the blood vessel wall before being diffused into the perisinusoidal space as marked by arrowhead in Fig. 3(b). Subsequently, the fluorescence signal in hepatocytes gradually increased, suggesting the absorption of free-form ICG or liposomal ICG by hepatocytes marked by asterisk in Fig. 3(b). For the free-form ICG, the liver sinusoid and hepatocytes were relatively well distinguished as the fluorescence signal in the liver sinusoid was significantly decreased after 2-3 minutes. On the other hand, for the liposomal ICG, the liver sinusoid and hepatocytes were less distinguishable as a significant portion of liposomal ICG kept circulating in the blood stream even after 5 minutes.

Figure 3(d) shows the fluorescence signal intensity in the hepatocytes of the liver, which was obtained by calculating the average of four different regions containing 1 or 2 hepatocytes. It continuously increased for 3 minutes and then became saturated for both of free-form ICG and liposomal ICG. As there was no clear difference in the initial absorption behavior to the hepatocytes between free-form ICG and liposomal ICG in the liver for the initial 5 minutes, we observed the liver again at later time point. Figure 3(e) shows the images acquired at 12 hours after the injection. No fluorescence signal in both of sinusoid and hepatocyte was detected in the liver of mouse received free-form ICG injection, suggesting complete hepatic clearance. In contrast, for the liver of mouse received liposomal ICG, small fluorescence signal was observed in the liver sinusoid (arrow) but not in the hepatocyte, suggesting a highly improved retention of liposomal ICG in blood circulation and clearance from the hepatocyte. In addition, interestingly, a highly accumulated fluorescence signal of ICG was observed in the Kupffer cell (arrowhead), the liver-resident macrophage, only in the liver of mouse injected with the liposomal ICG but not with the free-form ICG.

To further investigate the cellular pharmacokinetic of free-form and liposomal ICG in the liver, we used genetically-engineered cell type-specific fluorescence protein expressing mice, CD11c-YFP mice [35] and CX3CR1-GFP mice [36]. In the liver of CD11c-YFP mice, Kupffer cell and common dendritic cell can be visualized with CD11c associated expression of YFP [43]. In the liver of CX3CR1-GFP mice, inflammatory monocyte-derive macrophages and myeloid dendritic cells can be visualized with CX3CR1 associated expression of GFP [43]. Similar to the imaging results using wildtype BALB/c mice, no ICG fluorescence signal was observed in the liver of CD11c-YFP and CX3CR1-GFP mice at 24 hours after intravenous injection of free-from ICG. Figure 3(f) shows the images acquired from the liver of CD11c-YFP and CX3CR1-GFP mice at 24 hours after intravenous injection of liposomal ICG. In the liver of CD11c-YFP mice, most of the ICG fluorescence signal was co-localized with YFP expressing cell (arrow), suggesting phagocytosis of liposomal ICG by $CD11c^{+}$ Kupffer cell. In contrast, in the liver of CX3CR1-GFP mice, accumulated ICG fluorescence signal (arrowhead) was not co-localized with GFP expressing cell. It suggests that liposomal ICG was not phagocytized by $CX3CR1^{+}$ inflammatory monocyte-derive macrophages or liver-resident myeloid dendritic cells.

Biomedical Optics EXPRESS

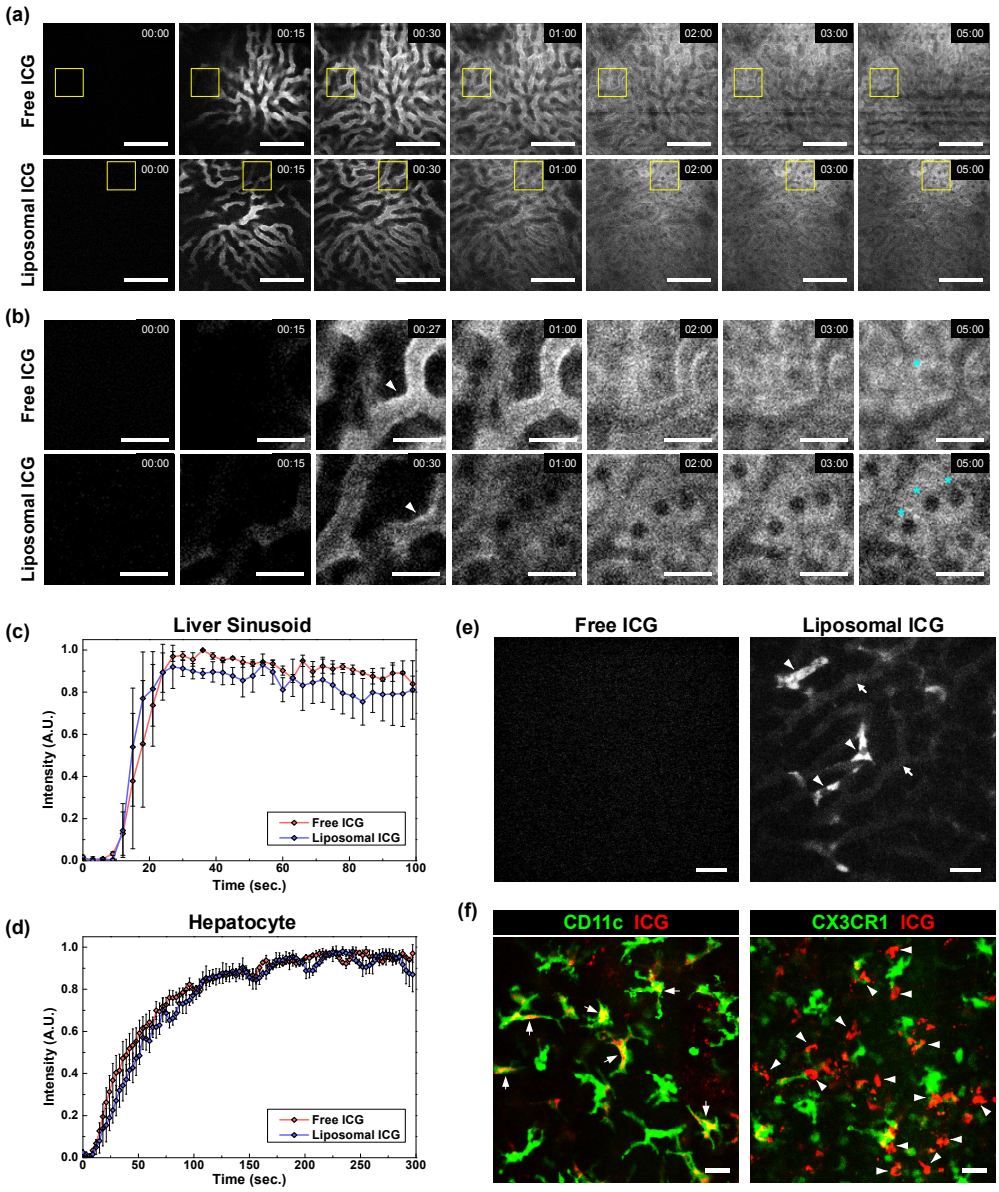

Fig. 3. (a) Representative sequential images of the liver of the mouse after intravenous injection of free-form or liposomal ICG, (Visualization 3 and Visualization 4). (b) Magnified sequential images at the area marked by yellow square in (a), (Visualization 5 and Visualization 6). (c, d) Relative fluorescence intensity in (c) liver sinusoid and (d) hepatocyte. (e) Images obtained at the liver at 12 hours after the intravenous injection of free-form and liposomal ICG. No fluorescence signal was observed in the liver of mouse received the free-form ICG injection. In the liver of mouse received liposomal ICG injection, fluorescence signal was observed in sinusoid (arrow) and Kupffer cell (arrowhead). (f) Images obtained at the liver of CD11c-YFP and CX3CR1-GFP mouse at 24 hours after intravenous injection of liposomal ICG. Scale bar: (a) 100 μm, (b, e-f), 25 μm.

4. Discussion

In this work, we built a video-rate confocal NIR laser-scanning microscopy for *in vivo* cellular-level monitoring of ICG, the FDA-approved biocompatible near infrared fluorophore.

Biomedical Optics EXPRESS

The real-time pharmacokinetic behaviors of intravenously injected free-form ICG and liposomal ICG were successfully visualized in a high spatiotemporal resolution in peripheral blood vessels and liver, *in vivo*.

With the real-time observation, the initial gradual mixing process of the intravenously injected ICG with the whole blood in circulation was clearly revealed in Fig. 2(b). A sharp spike of the fluorescence signal in the artery was observed at around 7 seconds after the intravenous injection of both of free-from ICG and liposomal ICG. It seems to be the revelation of the small portion of blood containing a relative high-concentration of the injected ICG that was created by the rapid bolus injection completed within 1 second, which is still in the process of gradual mixing with the whole blood. The smaller second peak representing the second circulation of the injected ICG through the whole body was observed at around 6 seconds after the first peak, which is closely matched to the known estimated blood circulation time of mouse whole body, 7 seconds [44]. The fluorescence signal in the vein started to appear after the initial spike of the fluorescence signal observed in the artery, suggesting the recirculation to the vein through the capillary network at the peripheral tissue. In our observation, it took more than 40 seconds for the small periodic fluctuation in the fluorescence signal to disappear, which suggests the completion of mixing process of the inject ICG with the whole blood. One of the major differences between the liposomal ICG and the free-form ICG in terms of pharmacokinetics is known to be an extended circulation in the blood stream. The observation of the blood-circulating fluorescence maintained as more than 30% of the peak intensity at 5 minutes after the intravenous injection of liposomal ICG shown in Fig. 2(b) is the result well consistent with the previous reports [21, 22].

Although the difference in the retention time of the free-form ICG and liposomal ICG in the blood stream is well-known, the difference in the liver absorbing the most of ICG from the blood circulation has only been partially analyzed, mostly in macroscopic scale not in cellular-level in real-time. In this work, we successfully monitored the initial perfusion of the free-form ICG and liposomal ICG into a liver sinusoid, diffusion into perisinusoidal space and absorption into hepatocytes (Visualization 3, Visualization 4, Visualization 5, and Visualization 6). We observed that the temporary accumulation of fluorescence at the boundary of the sinusoid, and then it gradually decreased as the fluorescence intensity in the hepatocytes increased. According to the known structure and metabolism process of the liver, the bright signal observed at the boundary of the sinusoid seems to be the space of Disse, the perisinusoidal space between a hepatocyte and a sinusoid; those diameter is only about 500 nm [45]. In the previous study, the excretion of green fluorescent sodium fluorescein from hepatocyte via bile duct, the main route of excretion, was monitored by two-photon microscopy [46]. However, in this study, the bile duct excretion was not clearly monitored as the optimal imaging plane of the bile duct is out of the confocal imaging plane of the hepatocyte, thereby the simultaneous real-time observation of them was difficult. To note, at 10 minutes after the intravenous injection, the bile duct excretion was clearly visible of both of free-form and liposomal ICG.

Notably, while we observed a significant retention of liposomal ICG in blood circulation both in blood vessels in the peripheral skin and liver sinusoid, we observed almost similar behaviors in initial absorption to hepatocyte for free-form ICG and liposomal ICG. It is unclear whether the portion of intact liposomal ICG was quickly absorbed to hepatocyte or the portion of liposomal ICG was immediately breached in blood circulation and the released ICG was absorbed in the similar pattern of free-form ICG. On the other hand, the difference of liposomal ICG in pharmacokinetics was clearly observed at 12 hours after injection; 1) the extended retention in liver sinusoid, and 2) accumulation in the liver-resident macrophage, Kupffer cell, supposedly by phagocytosis. This cellular uptake might be the result of a mononuclear phagocytic function of macrophage for the liposomal ICG. It could be a useful fluorescent labeling technique for *in vivo* observation of Kupffer cell in human as liposomal ICG is solely comprised of FDA approved biocompatible material, ICG and liposome.

Biomedical Optics EXPRESS

5. Conclusion

To summarize, we demonstrated that the microscopic-scale real-time pharmacokinetics of free-form ICG and liposomal ICG can be monitored *in vivo* using the custom-built video-rate near infrared confocal laser scanning microscopy. We successfully visualized the initial perfusion into the blood circulation, clearance from the blood stream after gradual mixing with whole blood, diffusion into the hepatic perisinusoidal space, and subsequent absorption into the hepatocyte *in vivo* in real time. This method can be a useful tool to investigate the real-time *in vivo* hepatic pharmacokinetics of intravenously administered biomaterials such as nanoparticles or pre-clinical drugs integrated with a near infrared fluorophore such as ICG.

Funding

This work was supported by the Global Frontier Project (NRF-2013M3A6A4044716) of National Research Foundation of Korea funded by the Ministry of Science, ICT and Future Planning (MSIP), and the Korea Healthcare Technology R&D Project funded by Ministry of Health and Welfare (HN12C0063, HI13C2181, HI15C0399).

Acknowledgments

The authors would like to thank Howon Seo, Eunjoo Song and Soo Yun Lee (KAIST) for their help on this project.

Disclosure

The authors declare that there are no conflicts of interest related to this article.